Please cite this article as:

A. Romero, J.A. Jiménez-Tejada, J. González, M.J. Deen, Unified electrical model for the contact regions of staggered Thin Film Transistors, Organic Electronics, (2021), 92, 106129.

©2021. This manuscript version is made available under the CC-BY-NCND 4.0 license

http://creativecommons.org/licenses/by-nc-nd/4.0/

Digital Object Identifier:
10.1016/j.orgel.2021.106129

Source:
https://www.sciencedirect.com/science/article/abs/pii/S1566119921000665?via%3Dihub

Unified electrical model for the contact regions of staggered Thin Film Transistors ☆

A. Romero[a], J. A. Jiménez-Tejada[a,*], J. González[b], M.J. Deen[c]

[a]*Departamento de Electrónica y Tecnología de Computadores, CITIC-UGR, Universidad de Granada, Granada 18071, Spain*
[b]*Departamento de Arquitectura y Tecnología de Computadores, CITIC-UGR, Universidad de Granada, Granada 18071, Spain*
[c]*Department of Electrical and Computer Engineering, McMaster University, 1280 Main Street West, Hamilton, Ontario L8S 4K1, Canada*

Abstract

In this work, we propose an unified compact model, which includes the effects of both source and drain contact regions, to describe the electrical characteristics of staggered thin film transistors (TFTs). The model is based on a generic drift analytical expression that describes the intrinsic channel of the transistor. Despite the distributed two-dimensional nature of the contacts in staggered configurations, two-terminal components are usually preferred to model the source and drain contact regions. In this regard, a model based on versatile simple expressions that describe the current-voltage relations of both contact regions are proposed in this work. These expressions are based on the physics underlying a metal-organic-metal structure. They can be adapted to different transport conditions, such as ohmic, space-charge-limited transport or Schottky-like contacts. This adaptation is controlled with the value of a single parameter that modifies the concavity or convexity of these expressions. The model works together with an evolutionary parameter extraction procedure, presented in a previous work for TFTs with negligible drain contact effects, and adapted here to this proposed model for staggered transistors. The results of the model and the evolutionary procedure have been validated with published experimental data of different TFTs, mostly organic thin film transistors (OTFTs). The model and evolutionary procedure agrees with other procedures tested successfully in the literature which were defined to cope with specific kinds of contacts in the TFTs. In this regard, our model and evolutionary parameter extraction procedure unify these previous procedures.

Keywords: Compact modeling, contact resistance, evolutionary parameter extraction method, modeling contact effects, thin-film transistors (TFTs)

1. Introduction

OTFTs are essential building blocks for the organic electronics, which are actively pursued for low-cost, large-area applications such as wearable and disposable electronic devices, flexible displays, sensors and logic circuits. The OTFT is a field-effect transistor (FET), with electrical characteristics similar to a MOSFET. However, compared with the crystalline-semiconductor counterparts, OTFTs have two serious performance limitations: a poor charge transport and a large voltage drop at the contact regions. This last limitation strongly affects short channel-length transistors. Therefore, efforts to achieve better static and dynamic OTFT performance are continually being researched [1, 2].

In OTFTs, free charges injected through the source are transported along three main regions of the device: the intrinsic or accumulation channel located in the organic material and close to the gate insulator, and the two contact regions located in the semiconductor close to the source and drain electrodes. OTFTs are usually fabricated in two different configurations: coplanar and staggered. In the first one, the source and drain electrodes and the intrinsic channel are aligned in parallel to the gate insulator. In the second case, the source and drain electrodes and the intrinsic channel are located on opposite sides of the organic layer.

In OTFTs, much attention has been paid in the past to describe the contact effects in OTFTs and to include these effects in the transistor's electrical model in order to accurately reproduce the experimental current-voltage characteristics of both staggered [3–7] and coplanar [8–21] devices. Overall, the voltage drop at the contacts of OTFTs is dominated by the source electrode as potentiometry measurements showed in Ref. [22]. This simplifies the modeling and characterization of OTFTs since the voltage drop at the drain contact is negligible and no parameters associated with this contact are necessary. However, this is not always the case, as was detected in staggered configurations with thick semiconductor layers [3, 4, 23].

In staggered configurations, current crowding occurs and the main contribution to the contact resistance can come from the bulk region far from the metal-semiconductor contact [24]. In these cases, the voltage drop at the drain contact region can be the same as the voltage drop at the source contact, and even greater for much thicker semiconductors [3]. The analysis of these OTFTs is more complex since the drain and source contact regions do not affect the electrical characteristics of the

☆This work was partially financed by the Consejería de Economía y Conocimiento de la Junta de Andalucía and European Regional Development Fund (ERDF) under project A-TIC-117-UGR18".

*Corresponding author.
Email addresses: ad90ry@correo.ugr.es (A. Romero), tejada@ugr.es (J. A. Jiménez-Tejada), jesusgonzalez@ugr.es (J. González), jamal@mcmaster.ca (M.J. Deen)

transistor in the same way. Actually, the saturation drain current of an OTFT is affected only by the intrinsic OTFT parameters and the source contact, but not by the drain contact [7].

The inverted staggered [bottom-gate top-contact (TC)] configuration is known to provide better performance than the inverted coplanar [bottom-gate botom-contact (BC)] structure [25, 26]. Numerical simulations and experimental works showed that the inverted staggered structure has a lower contact resistance than the inverted coplanar structure [25–29]. Nevertheless, most OTFTs have been fabricated in BC configurations because of the process difficulty of making source/drain (S/D) metal electrodes on top of the organic semiconductor layer with precise patterning [30, 31]. Recent advances on inkjet contact metallization on printed polymer semiconductors can reverse this trend in favor of staggered TFTs [32]. In order to be prepared for this scenario, a proper model to describe the staggered configuration is necessary, despite it being more complex model with more parameters.

So far, there are many approaches to describe the staggered configuration as well as different transport mechanisms that affect the contact region. These mechanisms include ohmic transport, space-charge-limited transport or injection-limited transport. In addition, the gate-voltage dependence of the carrier mobility and the contact resistance result in different modeling proposals [3–7].

Our aim is not to propose one additional model for staggered OTFTs, but to to integrate the existing ideas in one single model that is compatible with the coplanar configurations. Our motivation is from a recent observation by some researchers which stating that the lack of a standard compact model, which effectively brings together the device- and system-level development, is one of the reasons why the OFET technology remains at a relatively low technological level [33]. Nevertheless, a versatile model for the contact region of OTFTs was recently developed and tested in both coplanar and staggered OTFT configurations in which the voltage drop at the drain contact is negligible [20]. It reproduces the behavior of Schottky-barrier, space-charge-limited and ohmic contacts. It was incorporated in a generic analytical model that describes the current-voltage characteristics of OTFTs, and it is associated with an evolutionary parameter extraction method. However, this model poses some limitations when analyzing staggered configurations in which the drain contact resistance (R_D) can not be ignored.

In this work, we use this model and its associated evolutionary parameter extraction method [20] as a starting point, in which ideas extracted from previous models of staggered OTFTs are now incorporated.

2. Models for staggered OTFTs

Very often, authors propose to divide the source and drain contact regions of staggered OTFTs into two different parts, an access region, close to the metal organic interface whose electrical behavior is gate-voltage independent, and a farther region from this interface but close to the intrinsic channel which does depend on the gate voltage [3, 5, 6, 34]. Nevertheless, their approaches to model the electrical characteristics of the OTFTs

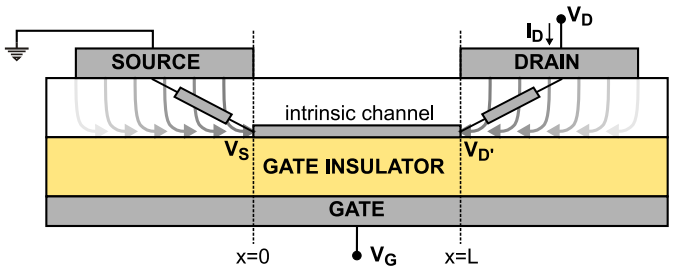

Figure 1: Schematic of inverted-staggered TFTs. The values of the gate-terminal voltage (V_G), and the drain-terminal voltage (V_D) are referred to the source-terminal voltage (ground). The active layer is divided into three regions: the source region, the intrinsic-channel region, and the drain region. Each region is modeled in this work with a two-terminal element, avoiding the 2D character of the source–drain current, illustrated with arrows.

differ. Some authors model the contact regions with linear components [3, 6] or with non-linear ones [5]. In this last case [5], the authors divided the access region into two parts in order to distinguish between charge injection (described with a power law) and space-charge-limited transport (described with Child's law). The charge injection is assumed to occur only from the source contact, and not from the drain contact [5].

Most of the approaches consider independent models for the source and drain contact regions [3–5]. Other approaches gather the effects of both the source and drain contacts into a unique contact resistance, in order to pay attention to a power-law dependence with the gate voltage of both the carrier mobility and the contact resistance [6]. Other authors do not distinguish between access and bulk regions [4], but pay special attention to the distributed effect of the current crowding in the contact region. They divide it as a parallel combination of conducting vertical channels that connect the top (bottom) contact with the intrinsic channel which lies horizontally on the bottom (top) part of the device [4]. In that work, the transport in any of these elemental vertical channels was attributed to a space-charge-limited regime. Interestingly, the results of this distributed model are explained later by using the contact resistance concept. As a consequence of their non-linear distributed model, the drain and source contact resistances vary with the drain voltage [4].

The reduction of a distributed two-dimensional (2D) model for the contact region into a 1D model, in which the contact region is seen as a two-terminal element is extensively found in the literature [6–8, 35–38]. This approach greatly simplifies the overall electrical model of the transistor. This two-terminal element can be a resistor [6], and also a non-linear component in case the current-voltage characteristics of the contact region are non-linear [7].

With these ideas in mind, we consider the staggered configuration of Figure 1 divided into three parts, and each part is described with a two-terminal component. Two of them model the current-voltage characteristics of the source and drain contact regions, and the third one models the intrinsic-channel.

2.1. Model for the intrinsic-channel

This last region is usually described with a generic charge drift model as [8, 10, 17, 19, 23, 38–43]:

$$I_D = k_0 \frac{W}{L} \frac{V_{EODR}(V_G, V_S)^{(2+\gamma)} - V_{EODR}(V_G, V_{D'})^{(2+\gamma)}}{2+\gamma},$$
$$k_0 = \mu_0 C_{ox};\ V_{EODR}(V_G, V) = V_{SS} \ln\left[1 + \exp\left(\frac{V_G - V_T - V}{V_{SS}}\right)\right], \quad (1)$$

which includes an electric field dependent mobility

$$\mu = \mu_0 (V_G - V_T)^{\gamma}, \quad (2)$$

with V_T being the threshold voltage, V_G the gate terminal voltage, and V_S and $V_{D'}$ are the values of the potential at the edges of the intrinsic channel in contact with the source and drain regions, respectively. Thus, V_S is the voltage drop at the source contact and $V_{DD'} = V_D - V_{D'}$ is the voltage drop at the drain contact (Fig. 1). W and L are the channel width and length, respectively, and C_{ox} the capacitance per unit area of the gate insulator. V_{SS} is a voltage parameter related to the steepness of the subthreshold region of the TFT, μ_0 is the mobility-related parameter expressed as $\mathrm{cm}^2/(\mathrm{V}^{1+\gamma}\mathrm{s})$, and γ is the mobility enhancement factor, suggested to depend on the characteristic energy width $E_0 = kT_0$ of an exponential tail distribution of the density of states (DOS) and the absolute temperature T, and $\gamma = 2(T_0/T - 1)$ [44]. In order to provide a single value for the voltage dependent mobility, the mobility is evaluated at $V_{GT} = V_G - V_T = 1$ V, thus $\mu(V_{GT} = 1\ \mathrm{V}) = \mu_0$ in $\mathrm{cm}^2/(\mathrm{Vs})$. This compact model is able to describe all operation modes of the transistor: triode, saturation, subthreshold or even reverse biasing.

In order to compute the model for the intrinsic channel (1), the voltage drop at the source and drain contacts, $V_S = V_S(I_D, V_G)$ and $V_{DD'} = V_{DD'}(I_D, V_G, V_D)$, respectively, must be known. In the following sections, models for these relations $V_S = V_S(I_D, V_G)$ and $V_{DD'} = V_{DD'}(I_D, V_G, V_D)$ are presented.

2.2. Model for the injection electrode

Models that describe the current-voltage characteristics of the source contact region has been studied in OTFTs in which the source contact region is dominant. A versatile model that is capable of describing both space-charge-limited transport in low energy contact-barriers [13] and injection-limited transport in Schottky barriers [38, 45–47] was recently proposed in [20]. The model is reduced to the following simple expression:

$$I_D = M_S \times {V_S}^{m_s},$$
$$\forall m_s \in \mathbb{Z} : 0 < m_s \leq 2, \quad (3)$$

where the value of the parameter m_s makes the model (3) discern between space-charge-limited transport [$1 \leq m_s \leq 2$, with (3) being a concave function] and injection-limited transport in Schottky barriers [$0 < m_s < 1$, with (3) being a convex function]. Two particular values are $m_s = 2$, in which (3) reduces to the classical Child's law; and $m_s = 1$, in which I_D and V_S are linearly related and the contact is ohmic:

$$I_D = V_S / R_S. \quad (4)$$

In this last case, the parameter M_S coincides with the contact conductance: $M_S = 1/R_S$, and M_S is usually gate-voltage dependent. Works analyzing ohmic contacts [6] or non-linear ones justify this dependence with the gate voltage [13]. In OTFTs free of hysteresis and local non-uniformities in the contact regions [11, 12, 15, 17–19], the next model is used to include the dependence of M_S with V_G: [13]:

$$M_S = \alpha_s (V_G - V_T)^{1+\gamma}, \quad (5)$$

where α_s is a proportionality constant. The subthreshold regime can be incorporated into (5) by an asymptotically interpolation function [19]:

$$M_S = \alpha_s \left\{ V_{SS} \ln\left[1 + \exp\left(\frac{V_G - V_T}{V_{SS}}\right)\right]\right\}^{1+\gamma}. \quad (6)$$

Note that (5) can be rewritten as a linear function of V_G:

$${M_S}^{1/(1+\gamma)} = \alpha_s^{1/(1+\gamma)} V_G - \alpha_s^{1/(1+\gamma)} \widehat{V_T}, \quad (7)$$

where $\widehat{V_T}$ would be the estimation of V_T, in case values of ${M_S}^{1/(1+\gamma)}$, extracted from experimental data, could be represented as a function of V_G. Moreover, if device parameters were known and the value of V_S could be extracted from (1) as

$$V_S = V_G - V_T - V_{SS} \times \ln\left[\exp\left(\frac{\left(\frac{I_D L(\gamma+2)}{W k_0} + V_{EODR}(V_{D'})^{(\gamma+2)}\right)^{\frac{1}{\gamma+2}}}{V_{SS}}\right) - 1\right], \quad (8)$$

then, the value of V_S from (8) should coincide with the one calculated with model (3).

2.3. Model for the drain contact voltage

As mentioned above, the drain contact, like the source contact, when seen as a two-terminal component, can be described by different expressions depending on the dominant transport mechanism [4, 7]. However, unlike the source contact, no unique versatile function exists to be applied to any kind of drain contact. Versatile model (3) has been successfully tested for the source contact of OTFTs in which the drain contact voltage is negligible. Based in the source contact model (3), we propose a similar expression for the drain contact region:

$$I_D = M_D \times {V_{DD'}}^{m_d},$$
$$\forall m_d \in \mathbb{Z} : 0 < m_d \leq 2, \quad (9)$$

where m_d defines the degree of convexity ($0 < m_d < 1$) or concavity ($1 \leq m_d \leq 2$) of (9). The particular case $m_d = 1$ would correspond to an ohmic drain contact [4] and $1/M_D \equiv R_D$ would represent the drain contact resistance, and therefore:

$$I_D = V_{DD'} / R_D. \quad (10)$$

The drain and source contact resistances in staggered configurations were proposed to have two terms, in agreement with the current crowding model: a first one associated to a constant access resistance and a second one associated to a gate voltage

dependent bulk resistance [6]. The first is usually negligible except at high gate voltages as the gateable bulk resistance diminishes with the gate voltage [6, 48]. Note that the source contact conductance M_S (5)-(6) is a function on the gate voltage. This electric field dependence of M_S was physically justified for $1 \leq m_s \leq 2$ (space-charge-limited contacts) [13] and assumed and checked for $0 < m_s < 1$ (Schottky contacts) [20]. In agreement with these previous works, M_D in (9) is expected to have a similar gate voltage dependence as M_S. However, note that the electric field and gate-induced charges at the drain side is reduced as the drain voltage increases. Greater drain contact resistances than source contact resistances have been detected when the drain voltage increases, while keeping V_G as constant [4]. Thus, any dependence of M_D with the electric field should include a dependence with the difference $V_G - V_D$, or at least with $V_G - k_d V_D$, where $k_d \in [0, 1]$ is a modulating factor controlling the V_D-dependence of M_D. In this regard, we propose the following expression for the parameter M_D:

$$M_D = \alpha_d \left\{ V_{SS} \ln \left[1 + \exp\left(\frac{V_G - k_d V_D - V_T}{V_{SS}} \right) \right] \right\}^{1+\gamma}, \quad (11)$$

with α_d being a proportionality constant. As in the source contact region, the $V_{DD'}$ value computed with model (9) should be consistent with the $V_{DD'}$ value extracted from (1):

$$V_{DD'} = V_D - V_G + V_T + V_{SS} \times \ln \left[\exp\left(\frac{\left(V_{EODR}(V_S)^{(\gamma+2)} - \frac{I_D L(\gamma+2)}{W k_0} \right)^{\frac{1}{\gamma+2}}}{V_{SS}} \right) - 1 \right]. \quad (12)$$

3. Evolutionary Parameter Extraction Procedure

Once the model for staggered OTFTs has been presented, which consists of equations (1), (3) and (9), output and transfer characteristics of staggered devices can be calculated using the bisection method [49]. The computation procedure is described in [17, 50]. The next step is its validation with different OTFTs, aiming to reproduce published experimental measurements.

In order to compare experimental and numerical results, a parameter extraction procedure is needed. We consider an evolutionary parameter extraction procedure that was developed for OTFTs in which the drain contact effects were negligible [17, 19–21, 50]. It requires only one set of output characteristics to extract the device parameters. Moreover, it is used in combination with an open source evolutionary tool called ECJ (A Java-based Evolutionary Computation Research System) [51]. This tool has been run in a *Windows 10* PC with a Intel Core i7-8750H CPU (2.2GHz). It was executed using all cores (6 cores/12 threads).

This procedure is redefined to the new constraints that the drain contact region imposes, basically the adaptation to expressions (1), (3) and (9). For the sake of clarity, the main steps of this procedure are described below.

3.1. Individual Representation

The procedure is based on a set of experimental output characteristics $I_D = I_D(V_{G_i}, V_{D_j})$, where $i \in \mathbb{Z} : 1 \leq i \leq g$ and $j \in \mathbb{Z} : 1 \leq j \leq d$, and g and d are the total number of discrete values of V_G and V_D, respectively. The numerical estimation of I_D with (1), (3) and (9) is named $\widehat{I_D}(V_{G_i}, V_{D_j}, x)$; the numerical estimation of the voltage drop at the source contact region V_S with (8) is named $\widehat{V_S}(V_{G_i}, V_{D_j}, x)$; and the numerical estimation of the voltage drop at the drain contact region $V_{DD'}$ with (12) is named $\widehat{V_{DD'}}(V_{G_i}, V_{D_j}, x)$, where x is called individual of the population and is the set of parameters needed to compute (1), (3) and (9); (8); or (12).

Since the linear relation (7) was obtained assuming that the OTFT is free of local non-uniformities in the contact regions, then, the set of parameters included in this individual depends whether this condition is fulfilled or not. In the first case:

$$x = (k_0, \gamma, V_T, V_{SS}, m_s, \alpha_s, m_d, \alpha_d, k_d), \quad (13)$$

otherwise, the parameter M_S must be extracted for each V_G and M_S will be part of the individual x, instead of α_s:

$$x = (k_0, \gamma, V_T, V_{SS}, m_s, M_S(V_{G_1}), \ldots, M_S(V_{G_g}), m_d, \alpha_d, k_d). \quad (14)$$

Such distinction is not applied to the drain contact region due to the empirical meaning of (11) and the dependence of M_D on both V_G and V_D, which would make necessary the inclusion of $g \times d$ different parameters in the individual, and would slow down the extraction procedure [17].

3.2. Fitness Function

The evolutionary parameter extraction procedure solves a many-objective problem (MaOP) with three objectives, in order to find the values of the set of parameters in x:

(O_1) to minimize the error between the experimental values of $I_D(V_{G_i}, V_{D_j})$ and their estimation from (1), (3) and (9) $\widehat{I_D}(V_{G_i}, V_{D_j}, x)$;

(O_2) to minimize the error between the voltage drop in the source contact region $V_S(V_{G_i}, V_{D_j}, x)$ calculated from (3), and its estimation $\widehat{V_S}(V_{G_i}, V_{D_j}, x)$ extracted from (8).

(O_3) to minimize the error between the voltage drop in the drain contact region $V_{DD'}(V_{G_i}, V_{D_j}, x)$ calculated from (9), and its estimation $\widehat{V_{DD'}}(V_{G_i}, V_{D_j}, x)$ extracted from (12).

The *Normalized Root Mean Squared Error* (NRMSE) is used to estimate errors (O_1), (O_2) and (O_3)[52]:

$$\mathrm{NRMSE}(y, \hat{y}) = \sqrt{\frac{\sum_{z=1}^{w} (y_z - \hat{y}_z)^2}{\sum_{z=1}^{w} (y_z - \bar{y})^2}} \quad (15)$$

where y represents the data set that we want to accurately approximate, $\hat{y}$ is the estimation of y, w is the number of data samples in y, and $\bar{y}$ is the mean value of the complete data set y.

Thus, our minimization MaOP, named O, is defined as $O = (O_1, O_2, O_3)$, where

$$\begin{aligned} O_1(x) &= \mathrm{NRMSE}\left(I_D(V_{G_i}, V_{D_j}), \widehat{I_D}(V_{G_i}, V_{D_j}, x)\right), \\ O_2(x) &= \mathrm{NRMSE}\left(V_S(V_{G_i}, V_{D_j}, x), \widehat{V_S}(V_{G_i}, V_{D_j}, x)\right), \\ O_3(x) &= \mathrm{NRMSE}\left(V_{DD'}(V_{G_i}, V_{D_j}, x), \widehat{V_{DD'}}(V_{G_i}, V_{D_j}, x)\right), \\ & \forall i \in \mathbb{Z} : 1 \le i \le g, \forall j \in \mathbb{Z} : 1 \le j \le d \end{aligned} \tag{16}$$

Objective (O_1) allows us to accurately reproduce the experimental output and transfer characteristics with our model, using the parameters coded in x. Objectives (O_2) and (O_3) check whether the trend of the current-voltage curves at the contacts, $I_D - V_S$ and $I_D - V_{DD'}$, extracted from (8) and (12), respectively, along with the parameters coded in x, are physically valid. Note that this procedure reduces to the one previously developed in OTFTs with negligible drain contact effects, [20] by setting $V_{D'} = V_D$ ($V_{DD'} = 0$). In that situation, objective (O_3) is not necessary.

4. Results

The functionality of compact model for staggered TFTs with contact effects (1), (3) and (9) and its associated parameter extraction evolutionary procedure (Section 3) are now tested. Experimental $I - V$ characteristics of different TFTs are reproduced with our model. We have chosen staggered TFTs with different kinds of contacts which were described with different functional expressions in other publications [4, 23]. We show in this section that our model unifies the previous different models described so far.

4.1. Ohmic contacts

In this experiment, the measured $I - V$ characteristics of two different top-gate bottom-contact Zinc Oxide (ZnO) TFTs [23] are reproduced with our model. In both cases, the contacts show an ohmic behavior. However, in one transistor, a ZnO TFT with equal geometric overlaps between the gate-and-S/D electrodes the drain contact resistance is negligible. In the second transistor, both contacts show a symmetrical response. This is a ZnO TFT that replaces the gate-to-drain overlap with a geometric gate-to-drain gap (L_{GD}) in the channel (the analyzed case corresponds to $L_{GD} = 0$, zero-offset) [23, Fig. 1]. The S/D metal contacts are Ru/Ru and Ru/Au, respectively.

Both ZnO TFTs were concurrently fabricated on an isolated silicon/silicon oxide/silicon nitride wafer with a five-layer process. Ru (15 nm) and Au (12 nm) were successively deposited and patterned as the S/D bottom metal contacts. Subsequently, ZnO (20 nm thick) was grown as the active channel layer using thermal atomic layer deposition. The gate insulator was a deposited 10 nm thick hafnium oxide (HfO_2) layer. Ru (80 nm thick) was sputtered and patterned with lift off afterwards to form the gate. Both TFTs have a channel width and length of 50 and 32 μm, respectively. A complete description of the electrode deposition, substrate cleaning and surface passivation procedures can be found in Ref. [23].

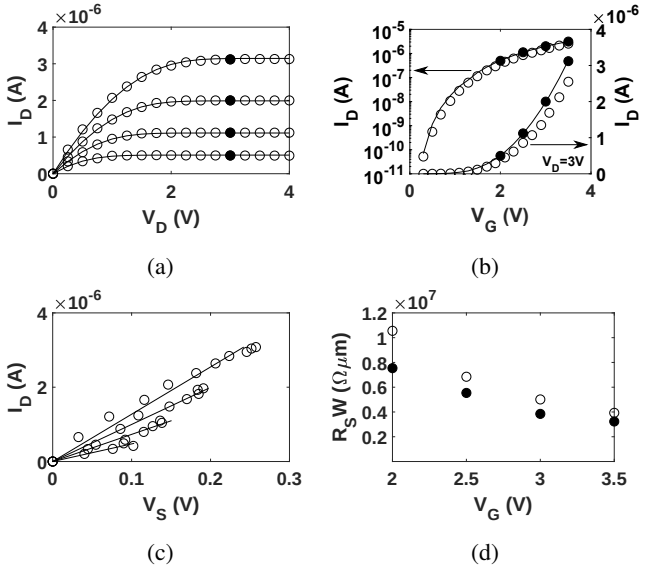

Figure 2: (a) Output and (b) transfer characteristics for a Ru/Ru staggered ZnO TFT (experimental data [23] shown with symbols and our calculations using (1), (3) and $V_{DD'} \approx 0$ with solid lines). The black circles of (a) and (b) are the same measurements. (c) Current–voltage curves extracted from (8) (symbols) and from (3) (solid lines). In (a) and (c), V_G is swept from 2 (bottom) to 3.5 V (top) with a 0.5 V step. (d) Width-normalized R_S values for the Ru/Ru staggered ZnO TFT extracted from our procedure (empty circles) and from [23] (solid circles).

4.1.1. Negligible drain contact

Here, the experimental output and transfer $I - V$ characteristics of the Ru/Ru staggered ZnO TFT are studied (symbols in Figs. 2a and 2b, respectively). The evolutionary procedure is applied to the $I_D - V_D$ curves shown with symbols in Fig. 2a.

The most accurate result provided by the evolutionary procedure is depicted with solid lines in Figs. 2a and 2b, showing a good agreement with experimental data (symbols). Note that the experimental transfer characteristics (open circles in Fig. 2b) and the experimental values extracted from the output characteristics (solid circles in Figs. 2a and 2b) differ a little. This may be due to charge trapping delays in the device. Also note that our procedure uses the experimental output characteristics to extract the parameters of the transistor. Thus, our calculations will fit better the solid circles than the open circles, which were measured in a separate experiment. The comparison of our calculations with experimental transfer characteristics is only to show the accuracy of our procedure. The parameters of the model extracted in this procedure are shown in Table 1. Note that no parameters related to the drain contact region appear in this table, since this solution converged to $V_{DD'} \approx 0$ (negligible drain contact effects). Regarding the source contact, the parameter M_S follows the trend given in (7). Thus, (13) was used, modeling the source contact with parameters m_s and α_s. The current–voltage curves extracted from the procedure are depicted in Fig. 2c [symbols if extracted with (8) and solid lines when extracted from (3)]. They are linear relations ($m_s = 1$). Thus, the source contact can be modeled by V_G-dependent resistances $R_S(V_G)$. These values are calculated with (6) and $R_S = 1/M_S$ and represented with empty circles in

Table 1: Extracted parameter sets for the Ru/Ru staggered ZnO TFT of Fig. 2.

x	This work	[23]
k_0 [A/V$^{2+\gamma}$]	7.19×10^{-07}	3.58×10^{-07}
γ	0.12	0.60
V_T [V]	0.93	0.54
V_{SS} [V]	0.363	0.161
m_s	1.00	–
α_s [A/V$^{2+\gamma}$]	4.43×10^{-06}	–

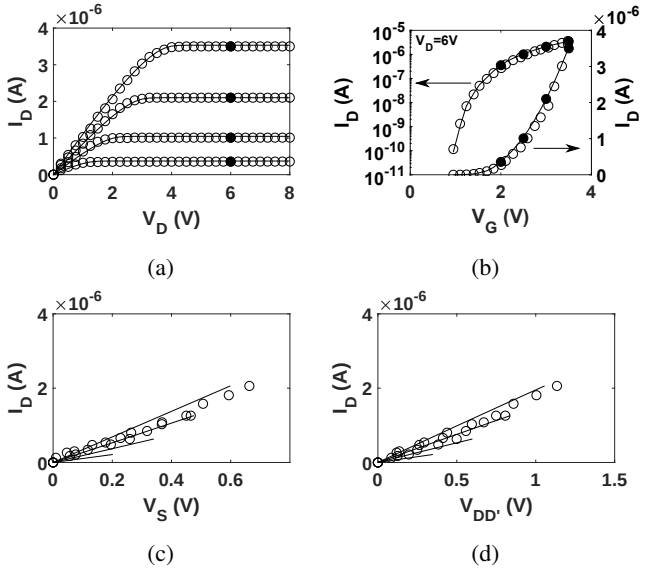

Figure 3: (a) Output and (b) transfer characteristics for a Ru/Au zero-offset TFT (experimental data [23] shown with symbols and our calculations using (1), (3) and (9) with solid lines). The black circles of (a) and (b) are the same measurements. (c) Current–voltage curves at the source contact extracted from (8) (symbols) and from (3) (solid lines). (d) Current–voltage curves at the drain contact extracted from (12) (symbols) and from (9) (solid lines). In (a), (c) and (d), V_G is swept from 2 (bottom) to 3.5 V (top) with a 0.5 V step.

Fig. 2d. The solid circles correspond to the values extracted in Ref. [23], showing a good agreement with our results. The values of remaining parameters (k_0, γ, V_T and V_{SS}) also agree with those obtained in [23] (also shown in Table 1). This agreement is not surprising, since both cases make use of (1) for the intrinsic channel, a resistor for the source contact region and a negligible drain contact resistance.

The small differences in the parameter values are only attributed to the extraction procedure. In [23], they modeled the contacts with parasitic transistors described with $I - V$ characteristics similar to (1) [23]. They have to discern whether the parasitic transistors operate in accumulation or fully depletion in order to simplify their analytical expressions of their model. Our search method automatically converges to the best solution, finds how the source and drain regions are operating, and extracts the $I_D - V_S$ curves, as represented in Fig. 2c.

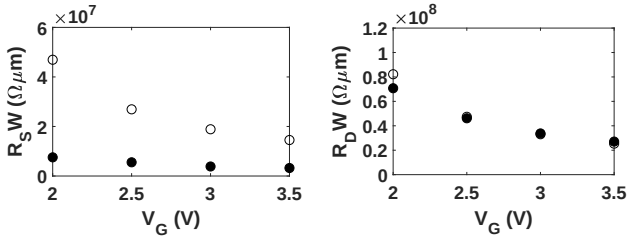

Figure 4: Width-normalized (a) source and (b) drain contact resistances as a function of the gate voltage for the Ru/Au zero-offset TFT. Our results are shown with empty symbols and those from [23] with solid symbols. R_D is evaluated at $V_D = 1$ V.

Table 2: Extracted parameter sets for the Ru/Au zero-offset ZnO TFT of Fig. 3.

x	This work	[23]
k_0 [A/V$^{2+\gamma}$]	3.43×10^{-06}	5.14×10^{-07}
γ	1.97×10^{-16}	0.40
V_T [V]	1.32	1.10
V_{SS} [V]	0.23	0.15
m_s	1.00	–
α_s [A/V$^{2+\gamma}$]	1.58×10^{-06}	–
m_d	1.00	–
α_d [A/V$^{2+\gamma}$]	9.14×10^{-07}	–
k_d	2.02×10^{-02}	–

4.1.2. Symmetrical source and drain contact effects

Next, we analyzed the experimental $I - V$ characteristics of the Ru/Au zero-offset TFT (Figs. 3a and 3b). The evolutionary procedure analyzes the experimental $I_D - V_D$ curves of Fig. 3a (symbols). The best fitting with solid lines in the same figure showed an excellent agreement. The parameter M_S is initially assumed to follow the trend given in (7). Thus, (13) is used, modeling the source contact with parameters m_s and α_s. The values of the extracted parameters are shown in Table 2 and the current-voltage curves at both contacts are shown in Figs. 3c and 3d. Both sets of curves are linear ($m_s = m_d = 1$). Thus, gate voltage dependent contact resistances can be determined. $R_S(V_G)$ can be obtained with (6) and $R_S = 1/M_S$ and $R_D(V_G, V_D)$ can be calculated with (11) and $R_D = 1/M_D$. They are represented with empty circles in Figs. 4a and 4b, respectively, with R_S being lower than R_D.

The R_S values determined with our procedure (empty symbols in Fig. 4a) are almost one order of magnitude greater than those obtained in [23] (solid symbols). This is consistent with the also greater value of the carrier mobility extracted with our method (5.544 cm^2/Vs) when compared with the one estimated in [23] (0.83 cm^2/Vs). Moreover, our result states that there is no V_G-dependence of μ ($\gamma \approx 0$), in contrast to Ref. [23] ($\gamma = 0.4$).

The values of the parameters V_T and V_{SS} are similar to the ones extracted in Ref. [23] (Table 2), and the values of the drain contact resistance R_D are almost identical (Fig. 4b).

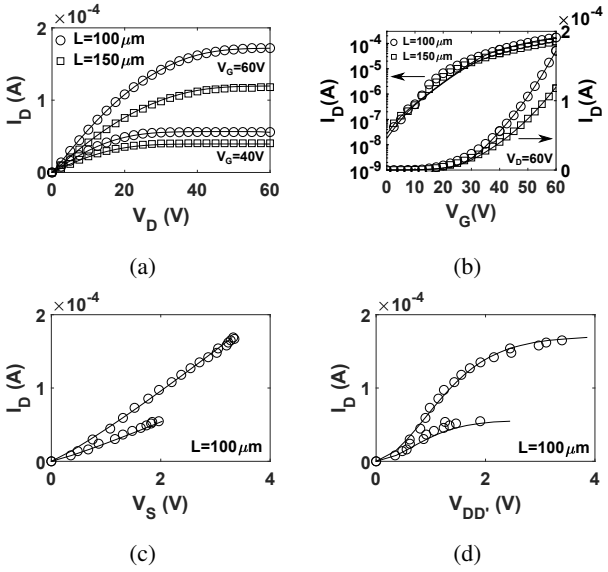

(a) (b) (c) (d)

Figure 5: (a) Output and (b) transfer characteristics of two pentacene OTFTs with different gate lengths (experimental data [4] shown with symbols and our calculations with (1), (3) and (9) with solid lines). (c) Current–voltage curves at the source contact extracted from (8) (symbols) and from (3) (solid lines) for the pentacene OTFT with $L = 100\ \mu m$. (d) Current–voltage curves at the drain contact extracted from (12) (symbols) and from (9) (solid lines) for the pentacene OTFT with $L = 100\ \mu m$. In (c) and (d), V_G is swept from 40 (bottom) to 60 V (top).

Table 3: Extracted parameter set for the pentacene OTFTs of Fig. 5.

x	Value
k_0 [A/V$^{2+\gamma}$]	7.99×10^{-09}
γ	0.099
V_T [V]	11.1
V_{SS} [V]	5.57
m_s	1.12
α_s [A/V$^{2+\gamma}$]	6.12×10^{-07}
m_d	1.71
α_d [A/V$^{2+\gamma}$]	1.22×10^{-06}
k_d	8.19×10^{-01}

This similarity is not surprising since our model and the one proposed in [23] are almost the same when analyzing ohmic contacts. Actually, the model for the source contact in [23] only allows for gate-voltage dependent source-contact resistances, since this region was modeled with a transistor working in accumulation. While these authors modeled the contact region with parasitic transistors, our model for the contact regions (3) and (9) is based on the theory of a metal-organic-metal structure [53]. The question is what happens when current voltage curves at the contacts differ from a linear relation. The application of our model to non-ohmic contacts is seen in the following sections.

4.2. Non linear contacts. Asymmetrical source and drain contact responses

In this experiment, we analyzed the experimental $I-V$ curves shown with symbols in Figs. 5a and 5b [4], corresponding to two pentacene inverted-staggered OTFTs with different channel lengths. The devices were fabricated using pentacene as the semiconducting layer in the OTFT. Heavily doped n-type Si was used both as a gate electrode and as a substrate, and a thermally grown SiO_2 layer and a spin coated polystyrene (PS) layer were used for the gate insulator. The pentacene film was deposited by thermal evaporation. Au was also thermally evaporated through the shadow mask in order to form the source and drain contacts. The capacitance per unit area of the gate dielectric layer is 1.4×10^{-08} F/cm^2. The full protocols of the electrode deposition, substrate cleaning, and surface passivation are in [4].

The authors in [4] studied the contact effects in these OTFTs, showing that both R_S and R_D impact the performance of the devices. These authors used a model for the intrinsic channel equivalent to (1). They considered the contact regions as a parallel combination of conducting vertical channels that connect the top contact with the intrinsic channel which lies horizontally on the bottom part of the device, for bottom-gate structures (or the bottom contact with the top part of the device, for top-gate configurations) [4]. In that work, the transport in any of these elemental vertical channels was attributed to space-charge-limited conduction. Interestingly, the results of this distributed model are explained later by using the contact resistance concept. They did not propose any explicit relation between the drain current and the voltage drop at the contact regions. However, they estimated the contact resistances in both the source and drain regions. As a consequence of their non-linear distributed model, the drain and source contact resistances clearly vary with the drain voltage [4].

Here, we use a two-terminal non-linear component concept to model the contact regions (see (3) and (9)). The evolutionary procedure is applied to the $I_D - V_D$ curves of the shortest pentacene OTFT ($L = 100\ \mu$m) [4]. Then, we check that the experimental $I - V$ characteristics of the longest pentacene OTFT ($L = 150\ \mu$m) can also be reproduced with our model and the parameters extracted with the shortest transistor.

The best solution of the evolutionary procedure is depicted with solid lines in Figs. 5a and 5b, showing a good agreement with the experimental data (symbols). The parameters of the model used in this calculation are shown in Table 3. Note that both source and drain contact regions play an essential role in the device performance. Regarding the source contact, the parameter M_S follows the trend given in (7). Thus, (13) was chosen to represent the individuals, modeling the source contact with parameters m_s and α_s. Non-linear transport in both contact regions is detected in the current-voltage curves ($I_D - V_S$ in Fig. 5c and $I_D - V_{DD'}$ in Fig. 5d), with $m_s = 1.12$ and $m_d = 1.71$, respectively.

In order to compare our results and the ones provided in [4], we determine the values of the source and drain contact resistances as $R_S(V_G, V_D) = V_S/I_D$ and $R_D(V_G, V_D) = V_{DD'}/I_D$, re-

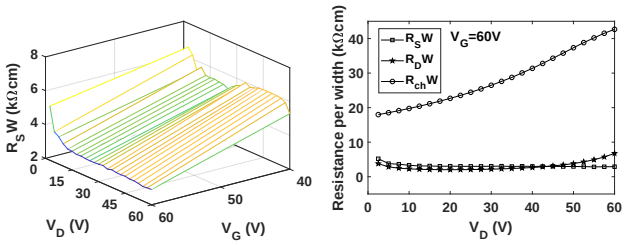

(a) (b)

Figure 6: (a) Width-normalized source contact resistance as a function of V_G and V_D for for the pentacene OTFTs of Fig. 5. (b) Comparison of the width-normalized channel, source- and drain-contact resistances ($R_{ch}W$, $R_S W$ and $R_D W$) for the pentacene OTFTs of Fig. 5.

spectively. Their width normalized values, including the channel resistance, $R_{ch} = (V_{D'} - V_S)/I_D$, are represented in Fig. 6. The values of $R_S W$ in the range 40 V $\leq V_G \leq$ 60 V and 0 V $\leq V_D \leq$ 60 V are represented in Fig. 6a. It can be seen that $R_S W$ varies from 2.85 to 6.58 kΩcm, which coincides with the values represented in [4, Fig. 6]. The dependence of R_S with V_G and V_D coincide too. On the one side, R_S decreases with increasing the gate voltage, because an increased number of induced charges both in the channel and in the source contact. On the other side, R_S decreases with increasing V_D at low values of V_D due to the concavity character of (3) when $1 \leq m_s \leq 2$, which models a space-charge-limited transport at the contact region.

In Fig. 6b, R_S, R_D and R_{ch} are depicted together as a function of V_D in the range $[0, 60]$ V and $V_G = 60$ V. R_S and R_D follow the same trend up to high values of V_D, in which R_D is greater than R_S, because the gate-induced charges at the drain side are lower than at the source side. The values of the resistances and this trend agree with the ones presented in [4, Fig. 8]. The values of the threshold voltage and mobility extracted in this work are also similar to those found in [4]. This agreement shows (i) the validity of our two-terminal non-linear contact model [(3) and (9)] in order to describe the contact regions of a staggered TFT; (ii) shows its analogy with a 2D model consisting of a distribution of channels connecting the electrodes and the intrinsic channel of the transistor [4]; and (iii) validates the metal-organic contact theory underlying our contact model (3) and (9).

4.3. Non linear contacts. Symmetrical source and drain contact responses

Our evolutionary procedure is applied to the measured output characteristics of an inverted staggered p-channel dinaphtho[2,3-b:2',3'-f]thieno[3,2-b]thiophene (DNTT) OTFT [7] with $L = 4$ μm and $W = 200$ μm, depicted with symbols in Fig. 7a. The OTFT was fabricated on flexible polyethylene naphthalate (PEN) substrates. Aluminum gate electrodes were deposited in vacuum. It uses a AlO_x/SAM hybrid gate dielectric with a capacitance per unit area 0.7 μF/cm^2. 25 nm thick gold source and drain contacts were deposited in vacuum conditions. The complete description of the electrode deposition, substrate cleaning and surface passivation is found in [7].

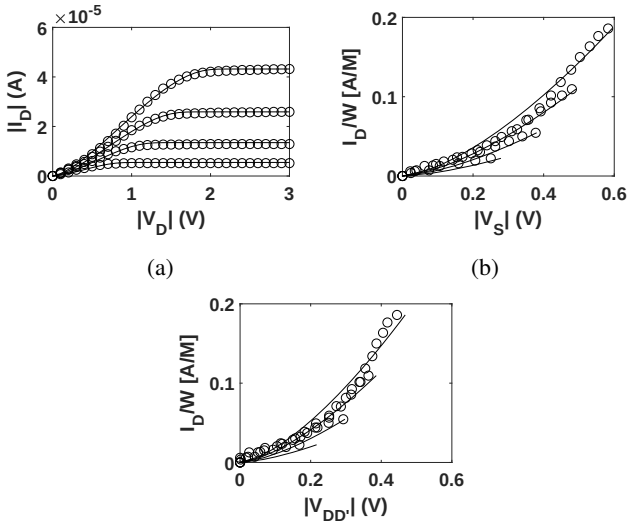

(a) (b)

(c)

Figure 7: (a) Output characteristics of a 4μm-channel-length DNTT OTFT (experimental data [7] shown with symbols and our calculations using (1), (3) and (9) with solid lines). (b) Current–voltage curves at the source contact extracted from (8) (symbols) and from (3) (solid lines). (c) Current–voltage curves at the drain contact extracted from (12) (symbols) and from (9) (solid lines). V_G is swept from −2.1 (bottom) to −3.0 V (top) with a −0.3 V step.

The best result of the evolutionary procedure is depicted with solid lines in Fig. 7a, showing a good agreement with the experimental data (symbols). The parameters of the model used in this calculation are shown in Table 4. Note that both source and drain contact regions play a symmetrical role in the device's performance. Regarding the source contact, the parameter M_S follows the trend given in (7). Thus, (13) was used as individual, modeling the source contact with parameters m_s and α_s. Non-linear transport in both contact regions is detected in the current-voltage curves ($I_D - V_S$ in Fig. 7b and $I_D - V_{DD'}$ in Fig. 7c), with $m_s = 1.51$ and $m_d = 1.49$, respectively).

The authors in [7] proposed a method to extract the current–voltage characteristics of the source and drain contacts. The intrinsic channel was modeled with (1), but neglecting the dependence of the mobility with the electric field ($\gamma = 0$). Note the low value of $\gamma = 0.13$ extracted with our procedure would validate the use of a negligible value for γ. Actually, their model was based on the ideal MOS model in which they incorporated empirical analytical models for the source and drain contact regions. These contact models are reverse-biased Schottky-diode expressions that fit current-voltage curves at the contacts that were previously extracted from experimental data. In the extraction of the current-voltage curves at the contacts, transistors with different channel lengths were used. The intrinsic parameters of the transistor were first determined from the long channel transistors. Then, they used transistors with different lengths and study the saturation region in order to characterize the source contact. Finally, the triode region provided information about the drain contact region. The reported $I_D - V_S$ and $I_D - V_{DD'}$ curves [7, Figs. 7a and 10] are identical to the ones extracted with our procedure and shown in Figs. 7b and 7c, re-

Table 4: Extracted parameter set for the 4μm-channel-length DNTT OTFT of Fig. 7.

x	Value
k_0 [A/V$^{2+\gamma}$]	2.27×10^{-06}
γ	0.135
V_T [V]	-1.43
V_{SS} [V]	9.03×10^{-02}
m_s	1.51
α_s [A/V$^{2+\gamma}$]	4.93×10^{-05}
m_d	1.49
α_d [A/V$^{2+\gamma}$]	6.95×10^{-05}
k_d	4.44×10^{-17}

spectively. The only difference is the expression used to model the contact regions: an exponential expression according to a reverse-biased Schottky-diode model in [7] instead of the potential functions used in (3) and (9). Also, the values $\mu_0 = 3.24$ cm^2/Vs, $V_T = -1.43$ V and $V_{SS} = 0.09$ V, extracted with our procedure, are quite similar to the same parameters reported in Ref. [7]. From [7], we highlight the idea of modeling both the drain and source contact regions and including the dependence with the gate voltage. Our proposal is to do this with a versatile model that can be valid in any type of contact (ohmic, Schottky or SCLC) and not using specific models for specific contacts. Also, we incorporated the dependence of the mobility with the electric field according to the VRH theory [54]. The great advantage of our method is that it requires exclusively one set of output characteristics, in order to extract the parameters of the transistor and the current-voltage curves at the contact regions.

4.4. Mott-Gurney source contacts and negligible drain contact effects

The final test analyzes the output characteristics of two different transistors showing pure Mott-Gurney source contacts and negligible drain contact effects.

4.4.1. Submicron-Channel-Length DNTT OTFT

The electrical characteristics measured in a staggered submicron-channel-length DNTT OTFT (symbols in Figs. 8a and 8b [55] are analyzed in this section. This device has a channel length of 0.5 μm, a channel width of 5 μm and a gate-to-contact overlap of 2 μm. It uses a AlO$_x$/SAM hybrid gate dielectric composed of a 3.6-nm-thick layer of aluminum oxide and a 1.7-nm-thick self-assembled monolayer (SAM) of n-tetradecylphosphonic acid. This hybrid gate dielectric has a capacitance per unit area of 700 nF/cm^2. A 25-nm-thick DNTT layer was deposited onto the AlO$_x$/SAM gate dielectric. A 30-nm-thick Au layer is deposited in vacuum to define the source and drain contacts. The electrode deposition, substrate cleaning and surface passivation descriptions are in Ref. [55].

The evolutionary procedure is applied to the $I_D - V_D$ curves of Fig. 8a. The best fitting obtained with the procedure is shown with solid lines in the same figure. A further validation of our procedure is shown in the fitting of the experimental transfer

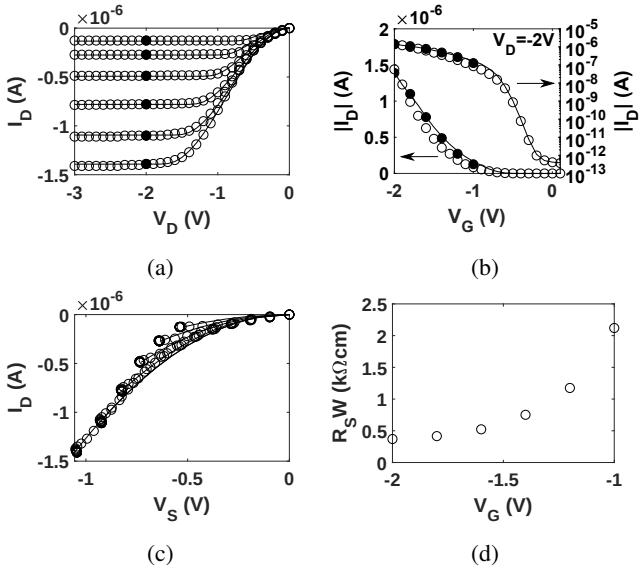

Figure 8: (a) Output and (b) transfer characteristics of a submicron-channel-length DNTT OTFT (experimental data [55] shown with circles and our calculations using (1), (3) and $V_{DD'} \approx 0$ with solid lines). The solid symbols in (a) and (b) are the same measurements. (c) Current–voltage curves extracted from (8) (symbols) and from (3) (solid lines). In (a) and (c), V_G is swept from -1 (top) to -2 V (bottom) with a -0.2 V step. (d) Width-normalized R_S for the submicron-channel-length DNTT OTFT at $V_D = -3$V.

Table 5: Extracted parameter set for the submicron-channel-length DNTT OTFT of Fig. 8.

x	Value
k_0 [A/V$^{2+\gamma}$]	5.69×10^{-07}
γ	8.44×10^{-06}
V_T [V]	-0.25
V_{SS}[V]	0.059
m_s	2.00
$M_S(-1.0V)$ [A/V^{m_s}]	4.66×10^{-07}
$M_S(-1.2V)$ [A/V^{m_s}]	6.77×10^{-07}
$M_S(-1.4V)$ [A/V^{m_s}]	9.18×10^{-07}
$M_S(-1.6V)$ [A/V^{m_s}]	1.14×10^{-06}
$M_S(-1.8V)$ [A/V^{m_s}]	1.27×10^{-06}
$M_S(-2.0V)$ [A/V^{m_s}]	1.26×10^{-06}

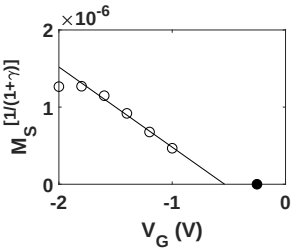

Figure 9: Extracted values of $M_S(V_{G_i})^{1/(1+\gamma)}$ (empty symbols) and V_T (solid symbol) for the submicron-channel-length DNTT OTFT. The solid line is the fitting with (5) of the five lowest points.

characteristics of Fig. 8b, in which a good agreement is seen

between the experimental data (symbols) and our calculations (solid lines). The solid circles in this figure were taken from the output characteristics of Fig. 8a. A slight difference in the experimental results is detected between the solid and open circles. Our calculations show a better agreement with the solid circles since the output characteristics were used in the evolutionary algorithm. The resulting parameters extracted after this fitting are shown in Table 5. In this case, the method converges to $V_{DD'} \approx 0$ ($R_S \gg R_D$). No solution was obtained if assuming that parameter M_S follows the trend given in (7), which suggests the existence of local non-uniformities near the contact region. For this reason, independent values of M_S for each value of V_G are searched. Thus, (14) was used as individual in the evolutionary algorithm. The values found for $M_S(V_G)$ are represented in Fig. 9. A linear trend is observed for small values of $|V_G|$ (solid line). At larger values of $|V_G|$, the linear trend (7) is lost. Different values for the threshold voltage were extracted with the evolutionary procedure ($V_T = -0.25$ V) and in Ref. [55] ($V_T = -0.7$ V). The value of the mobility extracted with our method ($\mu_0 = 0.81$ cm^2/Vs) is twice the value reported in Ref. [55], which was reported in the range [0.32, 0.41] cm^2/Vs. These differences can be attributed to the use of the transmission-line method (TLM), which requires multiple devices with different channel lengths to determine the contact resistance [56, 57]. TLM is only valid to determine the resistances of Ohmic contacts and for low drain biases, and it assumes that the contact region remains the same for all the transistors [58]. Nevertheless, these authors were aware of the huge effect of these short channel length transistors and that a greater value of the mobility should be expected, from measurements in longer DNTT OTFTs [59]. The severe non-linearity of the $I_D - V_D$ curves (Fig. 8a) for small V_D values, already noticed in [55], is confirmed here with the extraction of the current-voltage curves at the source contact (represented in Fig. 8c). The value $m_s = 2$ in (3) points out that the transport through the source contact follows the Mott-Gurney law.

4.4.2. [7]phenacene OTFT

Our model for staggered TFTs, (1), (3) and (9), is once more tested using the electrical characteristics of a p-type bottom-gate, top-contact [7]phenacene OTFT [60] (symbols in Figs. 10a and 10b). This device was fabricated on flexible poly(ethylene 2,6-naphthalate) (PEN) substrates using a narrow-gate multifinger architecture with $L = 20$ μm and $W = 4.03$ mm. The semiconductor layer has a thickness of 50 nm. Gold source and drain contacts were evaporated onto the semiconductor layer. The [7]phenacene OTFT has aluminum gate electrodes and a bilayer gate dielectric consisting of aluminum oxide (AlO_x), prepared by plasma oxidation, and an octadecylphosphonic acid ($C_{18}PA$) SAM, prepared in solution. The capacitance per unit area of the gate dielectric is 0.24 μF/cm^2. A complete description of the protocols of the electrode deposition, substrate cleaning and surface passivation is found in [60].

The best solution of the evolutionary procedure is shown with solid lines in Figs. 10a and 10b, showing a good agreement with the experimental data (symbols). The parameters of the model used in this calculation are shown in Table 6. In this case, the

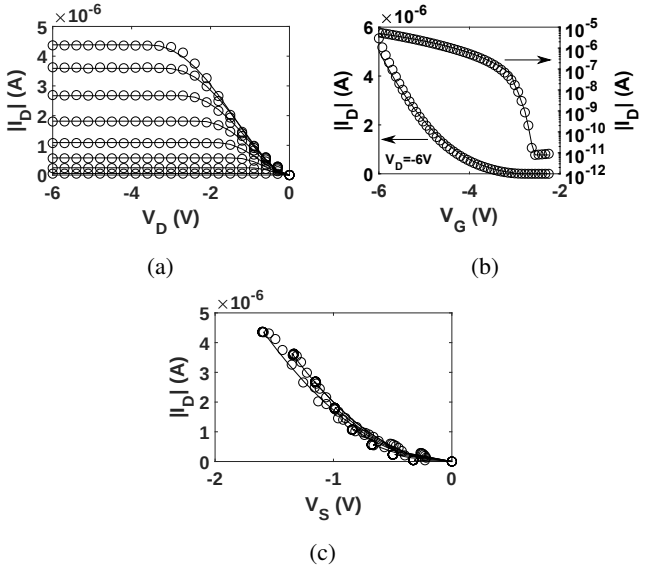

Figure 10: (a) Output and (b) transfer characteristics of a [7]phenacene OTFT (experimental data [60] shown with symbols and our calculations using (1), (3) and $V_{DD'} \approx 0$ with solid lines). (c) Current–voltage curves at the source contact extracted from (8) (symbols) and from (3) (solid lines). In (a) and (c), V_G is swept from −3 (bottom) to −6 V (top) with a −0.43 V step.

Table 6: Extracted parameter set for the [7]phenacene OTFT of Fig. 10.

x	Value
k_0 [A/V$^{2+\gamma}$]	1.10×10^{-08}
γ	0.105
V_T [V]	−2.44
V_{SS} [V]	3.11×10^{-02}
m_s	2.00
$M_S(-3.00V)$ [A/V^{m_s}]	5.00×10^{-07}
$M_S(-3.43V)$ [A/V^{m_s}]	1.02×10^{-06}
$M_S(-3.86V)$ [A/V^{m_s}]	1.29×10^{-06}
$M_S(-4.29V)$ [A/V^{m_s}]	1.57×10^{-06}
$M_S(-4.72V)$ [A/V^{m_s}]	1.86×10^{-06}
$M_S(-5.15V)$ [A/V^{m_s}]	1.99×10^{-06}
$M_S(-5.57V)$ [A/V^{m_s}]	1.99×10^{-06}
$M_S(-6.00V)$ [A/V^{m_s}]	1.72×10^{-06}

method converges to $V_{DD'} \approx 0$ ($R_S \gg R_D$). No solution was obtained if assuming that parameter M_S follows the trend given in (7), which suggests the existence of local non-uniformities near the contact region. For this reason, independent values of M_S for each value of V_G are searched. Thus, (14) was used as individual in the evolutionary algorithm. The values found for $M_S(V_G)$ are represented in Fig. 11, showing that they do not follow the linear relation (7) for the whole range of V_G values.

The non-linear response of I_D for small V_D values reported in Ref. [60] is confirmed in the current-voltage curves at the source contact extracted with our procedure (Fig. 10c) with $m_s = 2$. The values $V_T = -2.44$ V and $\mu_0 = 0.05$ cm^2/Vs, extracted with our procedure, are slightly different to those obtained in [60], −3.3 V and 0.03 cm^2/Vs, respectively. This com-

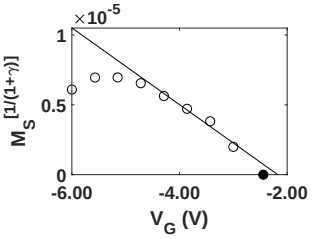

Figure 11: Extracted $M_S\,(V_{G_i})^{1/(1+\gamma)}$ (empty symbols) and V_T (solid symbol) values for the [7]phenacene OTFT. The solid line is fitting with (5) of the six lowest points.

parison is not complete since authors in Ref. [60] did not provide any information about the contact effects, which would alter the value of the other parameters.

An interesting fact from the two cases studied in this section with pure Mott–Gurney contacts ($m_s = 2$) is that $R_S \gg R_D$. In this regard, more effort should be devoted in studying these kind of contacts in case this situation is not fortuitous.

4.5. Other kind of contacts

In addition to these kinds of staggered OTFTs, the electrical characteristics of staggered OTFTs with other kinds of source contacts were successfully reproduced with the previous version of the model, which assumes a negligible drain contact [20]. In that work, the following cases were studied: non-linear ($1 < m_s < 2$) source contact and negligible drain contact effect in [20, Experiment C] and Schottky source contacts and negligible drain contact effect in [20, Experiment D].

4.5.1. Conclusions

A compact model for staggered thin film transistors including the effects of the source and drain contacts has been satisfactorily combined with an evolutionary parameter extraction procedure. The transistor parameters and the current-voltage curves at the contacts have been extracted in different transistors. The results have been compared with the results obtained with other procedures, designed specifically for particular transistors with particular behaviors at the contact regions. The good agreement between our results and the results obtained with these other models makes our model and evolutionary algorithm a versatile one to characterize any kind of staggered thin-film transistor.

Also, different kinds of contacts have been analyzed and reproduced with our model: ohmic contacts in which the drain contact is negligible, ohmic contacts with symmetrical source and drain contact effects, non-linear contacts with both symmetrical and asymmetrical source and drain contact effects, and pure Mott-Gurney source contacts with negligible drain contact effects. Thus, the key goal of this work, which was the compilation of many ideas and models, applied to different OTFTs with different contact behaviors, into one versatile model was demonstrated. A final remark should be make regarding the use of the evolutionary procedure. It is a tool that accelerates the search of a valid solution. However, expert knowledge is still necessary to manage any situation, in particular in the selection of the initial ranges of values of the different parameters. By avoiding this, the decision-making could be completely automated, and therefore, the procedure could be seen as an user-independent tool. In this sense, it is shown that a line of work is wide open, even to the use of other searching algorithms.

[1] J. W. Borchert, U. Zschieschang, F. Letzkus, M. Giorgio, R. T. Weitz, M. Caironi, J. N. Burghartz, S. Ludwigs, H. Klauk, Flexible low-voltage high-frequency organic thin-film transistors, Sci. Adv. 6 (21) (2020) eaaz5156.

[2] N. Firoz, B. Mazhari, Extraction of source resistance in thin film transistors using a single gated-probe outside the channel, J. Phys. D Appl. Phys. 53 (35) (2020) 355104.

[3] T. J. Richards, H. Sirringhaus, Analysis of the contact resistance in staggered, top-gate organic field-effect transistors, J. Appl. Phys. 102 (9) (2007) 094510.

[4] C. W. Sohn, T. U. Rim, G. B. Choi, Y. H. Jeong, Analysis of contact effects in inverted-staggered organic thin-film transistors based on anisotropic conduction, IEEE Trans. Electron Devices 57 (5) (2010) 986–994.

[5] A. Fischer, H. Zündorf, F. Kaschura, J. Widmer, K. Leo, U. Kraft, H. Klauk, Nonlinear contact effects in staggered thin-film transistors, Phys. Rev. Appl. 8 (5).

[6] S. Jung, J. W. Jin, V. Mosser, Y. Bonnassieux, G. Horowitz, A compact model and parameter extraction method for a staggered OFET with power-law contact resistance and mobility, IEEE Trans. Electron Devices 66 (11) (2019) 4894–4900.

[7] S. Elsaegh, U. Zschieschang, J. W. Borchert, H. Klauk, H. Zappe, Y. Manoli, Compact DC modeling of organic thin-film transistors including their parasitic non-linear contact effects based on a novel extraction method, IEEE Trans. Electron Devices 66 (11) (2019) 4907–4914.

[8] O. Marinov, M. J. Deen, U. Zschieschang, H. Klauk, Organic Thin-Film Transistors: Part I-Compact DC Modeling, IEEE Trans. Electron Devices 56 (2009) 2952–2961.

[9] M. J. Deen, M. H. Kazemeini, S. Holdcroft, Contact effects and extraction of intrinsic parameters in poly(3-alkylthiophene) thin film field-effect transistors, J. Appl. Phys. 103 (12) (2008) 124509.

[10] M. J. Deen, O. Marinov, U. Zschieschang, H. Klauk, Organic Thin-Film Transistors: Part II. Parameter Extraction, IEEE Trans. Electron Devices 56 (12) (2009) 2962 –2968.

[11] J. A. Jiménez-Tejada, K. M. Awawdeh, J. A. López-Villanueva, J. E. Carceller, M. J. Deen, N. B. Chaure, T. Basova, A. K. Ray, Contact effects in compact models of organic thin film transistors: Application to zinc phthalocyanine-based transistors, Org. Electron. 12 (5) (2011) 832–842.

[12] K. M. Awawdeh, J. A. Jiménez-Tejada, P. López-Varo, J. A. López-Villanueva, F. M. Gómez-Campos, M. J. Deen, Characterization of organic thin film transistors with hysteresis and contact effects, Org. Electron. 14 (12) (2013) 3286–3296.

[13] J. A. Jiménez-Tejada, J. A. López-Villanueva, P. López-Varo, K. M. Awawdeh, M. J. Deen, Compact modeling and contact effects in organic transistors, IEEE Trans. Electron Devices 61 (2) (2014) 266–277.

[14] F. Torricelli, M. Ghittorelli, L. Colalongo, Z.-M. Kovacs-Vajna, Single-transistor method for the extraction of the contact and channel resistances in organic field-effect transistors, Appl. Phys. Lett. 104 (9) (2014) 093303.

[15] J. A. Jiménez-Tejada, P. López-Varo, A. N. Cammidge, I. Chambrier, M. J. Cook, N. B. Chaure, A. K. Ray, Compact Modeling of Organic Thin-Film Transistors with Solution Processed Octadecyl Substituted Tetrabenzotriazaporphyrin as an Active Layer, IEEE Trans. Electron Devices 64 (6) (2017) 2629–2634.

[16] B. Li, C. Y. Han, P. T. Lai, W. M. Tang, Effects of source/drain-electrode material, thickness and fabrication method on the electrical performance of pentacene thin-film transistor, Thin Solid Films 667 (2018) 28 – 33.

[17] A. Romero, J. González, R. Picos, M. J. Deen, J. A. Jiménez-Tejada, Evolutionary parameter extraction for an organic TFT compact model including contact effects, Org. Electron. 61 (2018) 242 – 253.

[18] J. A. Jiménez-Tejada, P. Lopez-Varo, N. B. Chaure, I. Chambrier, A. N. Cammidge, M. J. Cook, A. Jafari-Fini, A. K. Ray, Organic thin film transistors using a liquid crystalline palladium phthalocyanine as active layer, J. Appl. Phys. 123 (11) (2018) 115501.

[19] A. Romero, C. Jiménez, J. González, P. López-Varo, M. J. Deen, J. A. Jiménez-Tejada, Compact modeling of the effects of illumination on the

contact region of organic phototransistors, Org. Electron. 70 (2019) 113 – 121.

[20] A. Romero, J. González, M. Deen, J. A. Jiménez-Tejada, Versatile model for the contact region of organic thin-film transistors, Org. Electron. 77 (2020) 105523.

[21] J. A. Jiménez-Tejada, A. Romero, J. González, N. B. Chaure, A. N. Cammidge, I. Chambrier, A. K. Ray, M. J. Deen, Evolutionary computation for parameter extraction of organic thin-film transistors using newly synthesized liquid crystalline nickel phthalocyanine, Micromachines 10 (10) (2019) 683.

[22] L. Bürgi, T. J. Richards, R. H. Friend, H. Sirringhaus, Close look at charge carrier injection in polymer field-effect transistors, J. Appl. Phys. 94 (9) (2003) 6129–6137.

[23] A. M. Ma, D. W. Barlage, Analysis of the Channel and Contact Regions in Staggered and Drain-Offset ZnO Thin-Film Transistors With Compact Modeling, IEEE Trans. Electron Devices 65 (8) (2018) 3277–3282.

[24] J. W. Borchert, B. Peng, F. Letzkus, J. N. Burghartz, P. K. L. Chan, K. Zojer, S. Ludwigs, H. Klauk, Small contact resistance and high-frequency operation of flexible low-voltage inverted coplanar organic transistors, Nat. Commun. 10 (1).

[25] I. Kymissis, C. Dimitrakopoulos, S. Purushothaman, High-performance bottom electrode organic thin-film transistors, IEEE Trans. Electron Devices 48 (6) (2001) 1060–1064.

[26] S. Scheinert, G. Paasch, Fabrication and analysis of polymer field-effect transistors, physica status solidi (a) 201 (6) (2004) 1263–1301.

[27] D. J. Gundlach, L. Zhou, J. A. Nichols, T. N. Jackson, P. V. Necliudov, M. S. Shur, An experimental study of contact effects in organic thin film transistors, J. Appl. Phys. 100 (2) (2006) 024509.

[28] C.-H. Shim, F. Maruoka, R. Hattori, Structural analysis on organic thin-film transistor with device simulation, IEEE Trans. Electron Devices 57 (1) (2010) 195–200.

[29] L. Feng, X. Xu, X. Guo, Structure-dependent contact barrier effects in bottom-contact organic thin-film transistors, IEEE Trans. Electron Devices 59 (12) (2012) 3382–3388.

[30] M. Mizukami, N. Hirohata, T. Iseki, K. Ohtawara, T. Tada, S. Yagyu, T. Abe, T. Suzuki, Y. Fujisaki, Y. Inoue, S. Tokito, T. Kurita, Flexible AM OLED panel driven by bottom-contact OTFTs, IEEE Electron Device Lett. 27 (4) (2006) 249–251.

[31] H. Matsui, K. Hayasaka, Y. Takeda, R. Shiwaku, J. Kwon, S. Tokito, Printed 5-v organic operational amplifiers for various signal processing, Sci. Rep. 8 (1).

[32] Y. Lee, J. Kwon, S. Jung, W. Kim, S. Baek, S. Jung, Reliable inkjet contact metallization on printed polymer semiconductors for fabricating staggered TFTs, Appl. Phys. Lett. 116 (15) (2020) 153301.

[33] S. Jung, Y. Bonnassieux, G. Horowitz, S. Jung, B. Iniguez, C.-H. Kim, Advances in compact modeling of organic field-effect transistors, IEEE J. Electron Dev. Soc. (2020) 1–1.

[34] F. Torricelli, E. C. P. Smits, J. R. Meijboom, A. K. Tripathi, G. H. Gelinck, L. Colalongo, Z. M. Kovacs-Vajna, D. M. de Leeuw, E. Cantatore, Transport physics and device modeling of zinc oxide thin-film transistors—part II: Contact resistance in short channel devices, IEEE Trans. Electron Devices 58 (9) (2011) 3025–3033.

[35] Z. Xie, M. S. A. Abdou, X. Lu, M. J. Deen, S. Holdcroft, Electrical characteristics and photolytic tuning of poly(3-hexylthiophene) thin film metal–insulator–semiconductor field-effect transistors (MISFETs), Can. J. Phys. 70 (10-11) (1992) 1171–1177.

[36] M. Deen, M. Kazemeini, Y. Haddara, J. Yu, G. Vamvounis, S. Holdcroft, W. Woods, Electrical characterization of polymer-based FETs fabricated by spin-coating poly(3-alkylthiophene)s, IEEE Trans. Electron Devices 51 (11) (2004) 1892–1901.

[37] P. V. Necliudov, M. S. Shur, D. J. Gundlach, T. N. Jackson, Modeling of organic thin film transistors of different designs, J. Appl. Phys. 88 (11) (2000) 6594–6597.

[38] A. Valletta, M. Rapisarda, S. Calvi, G. Fortunato, M. Frasca, G. Maira, A. Ciccazzo, L. Mariucci, A DC and small signal AC model for organic thin film transistors including contact effects and non quasi static regime, Org. Electron. 41 (Supplement C) (2017) 345–354.

[39] M. Fayez, K. M. Morsi, M. N. Sabry, OTFTs compact models: analysis, comparison, and insights, IET Circ. Device. Syst. 11 (5) (2017) 409–420.

[40] S. Abdinia, F. Torricelli, G. Maiellaro, R. Coppard, A. Daami, S. Jacob, L. Mariucci, G. Palmisano, E. Ragonese, F. Tramontana, A. van Roermund, E. Cantatore, Variation-based design of an AM demodulator in a printed complementary organic technology, Org. Electron. 15 (4) (2014) 904–912.

[41] R. Martins, D. Gaspar, M. J. Mendes, L. Pereira, J. Martins, P. Bahubalindruni, P. Barquinha, E. Fortunato, Papertronics: Multigate paper transistor for multifunction applications, Appl. Mater. Today 12 (2018) 402–414.

[42] M. Buonomo, N. Lago, G. Cantarella, N. Wrachien, M. Natali, F. Prescimone, E. Benvenuti, M. Muccini, S. Toffanin, A. Cester, Simple and accurate single transistor technique for parameters extraction from organic and inorganic thin film devices, Org. Electron. 63 (2018) 376–383.

[43] S. Fatima, U. Rafique, U. Ahmed, M. Ahmed, A global parameters extraction technique to model organic field effect transistors output characteristics, Solid-State Electron. 152 (2019) 81–92.

[44] O. Marinov, M. J. Deen, R. Datars, Compact modeling of charge carrier mobility in organic thin-film transistors, J. Appl. Phys. 106 (6) (2009) 064501.

[45] A. Valletta, A. Daami, M. Benwadih, R. Coppard, G. Fortunato, M. Rapisarda, F. Torricelli, L. Mariucci, Contact effects in high performance fully printed p-channel organic thin film transistors, Appl. Phys. Lett. 99 (23) (2011) 233309.

[46] L. Mariucci, M. Rapisarda, A. Valletta, S. Jacob, M. Benwadih, G. Fortunato, Current spreading effects in fully printed p-channel organic thin film transistors with schottky source–drain contacts, Org. Electron. 14 (1) (2013) 86–93.

[47] M. Charbonneau, D. Locatelli, S. Lombard, C. Serbutoviez, L. Tournon, F. Torricelli, S. Abdinia, E. Cantatore, M. Fattori, A Large-Area Gravure Printed Process for P-type Organic Thin-Film Transistors on Plastic Substrates, in: 2018 48th European Solid-State Device Research Conference (ESSDERC), IEEE, 2018, pp. 70–73.

[48] E. J. Meijer, G. H. Gelinck, E. van Veenendaal, B.-H. Huisman, D. M. de Leeuw, T. M. Klapwijk, Scaling behavior and parasitic series resistance in disordered organic field-effect transistors, Appl. Phys. Lett. 82 (25) (2003) 4576–4578.

[49] R. L. Burden, D. J. Faires, Numerical analysis, 3rd Edition, PWS Publishing Company, Boston, 1985.

[50] A. Romero, J. González, J. A. Jiménez-Tejada, Constrained Many-Objective Evolutionary Extraction Procedure for an OTFT Compact Model Including Contact Effects, in: 2018 Spanish Conference on Electron Devices (CDE), IEEE, 2018, pp. 1–4.

[51] S. Luke, ECJ evolutionary computation library, available for free at http://cs.gmu.edu/∼eclab/projects/ecj/ (1998).

[52] J. González, I. Rojas, J. Ortega, H. Pomares, F. Fernandez, A. Díaz, Multiobjective evolutionary optimization of the size, shape, and position parameters of radial basis function networks for function approximation, IEEE Trans. Neural Netw. 14 (6) (2003) 1478–1495.

[53] P. Lara Bullejos, J. A. Jiménez-Tejada, M. J. Deen, O. Marinov, W. R. Datars, Unified model for the injection and transport of charge in organic diodes, J. Appl. Phys. 103 (6) (2008) 064504.

[54] O. Marinov, M. Deen, J. Jiménez-Tejada, C. Chen, Variable-range hopping charge transport in organic thin-film transistors, Phys. Rep. 844 (2020) 1–105.

[55] U. Zschieschang, F. Letzkus, J. N. Burghartz, H. Klauk, Parameter uniformity of submicron-channel-length organic thin-film transistors fabricated by stencil lithography, IEEE Trans. Nanotechnol. 16 (5) (2017) 837–841.

[56] H. H. Berger, Contact resistance and contact resistivity, J. Electrochem. Soc. 119 (4) (1972) 507.

[57] U. Kraft, J. E. Anthony, E. Ripaud, M. A. Loth, E. Weber, H. Klauk, Low-voltage organic transistors based on tetraceno[2,3-b]thiophene: Contact resistance and air stability, Chem. Mater. 27 (3) (2015) 998–1004.

[58] F. Ante, D. Kälblein, T. Zaki, U. Zschieschang, K. Takimiya, M. Ikeda, T. Sekitani, T. Someya, J. N. Burghartz, K. Kern, H. Klauk, Contact resistance and megahertz operation of aggressively scaled organic transistors, Small 8 (1) (2011) 73–79.

[59] U. Kraft, K. Takimiya, M. J. Kang, R. Rödel, F. Letzkus, J. N. Burghartz, E. Weber, H. Klauk, Detailed analysis and contact properties of low-voltage organic thin-film transistors based on dinaphtho[2,3-b:2′,3′-f]thieno[3,2-b]thiophene (DNTT) and its didecyl and diphenyl derivatives, Org. Electron. 35 (2016) 33–40.

[60] A. A. Ruzaiqi, H. Okamoto, Y. Kubozono, U. Zschieschang, H. Klauk, P. Baran, H. Gleskova, Low-voltage organic thin-film transistors based on [n]phenacenes, Org. Electron. 73 (2019) 286–291.